Parity-violating hybridization in heavy Weyl semimetals

Po-Yao Chang[1,*] and Piers Coleman[1,2]
[1]*Center for Materials Theory, Rutgers University, Piscataway, New Jersey 08854, USA*
[2]*Department of Physics, Royal Holloway, University of London, Egham, Surrey TW20 0EX, United Kingdom*

(Received 2 November 2017; published 17 April 2018)

We introduce a simple model to describe the formation of heavy Weyl semimetals in noncentrosymmetric heavy fermion compounds under the influence of a parity-mixing, onsite hybridization. A key aspect of interaction-driven heavy Weyl semimetals is the development of surface Kondo breakdown, which is expected to give rise to a temperature-dependent reconfiguration of the Fermi arcs and the Weyl cyclotron orbits which connect them via the chiral bulk states. Our theory predicts a strong temperature-dependent transformation in the quantum oscillations at low temperatures. In addition to the effects of surface Kondo breakdown, the renormalization effects in heavy Weyl semimetals will appear in a variety of thermodynamic and transport measurements.

DOI: 10.1103/PhysRevB.97.155134

I. INTRODUCTION

Heavy fermion materials are a tunable class of compounds in which strong electron correlations give rise to a wealth of metallic, superconducting, magnetic, and insulating phases. A new aspect of these materials is the possibility of topological behavior, epitomized by the topological Kondo insulator (TKI) SmB_6 [1–6], in which a topologically nontrivial entanglement between local moments and conduction electrons, gives rise to Dirac surface states [7–10]. An important second class of topological behavior occurs in the presence of broken inversion or time-reversal symmetry, which transforms the quantum critical point between normal and topological insulators into a Weyl semimetal phase, with relativistic chiral fermions in the bulk and Fermi arc states [11–13] on the surface. Various Weyl semimetallic phases have been proposed and discovered in weakly interacting systems [14–16]. Most Weyl semimetals are noncentrosymmetric crystals [11].

A preponderance of noncentrosymmetric heavy fermion materials offers an exciting opportunity to explore strongly interacting, or "heavy Weyl semimetals" (hWSMs) [17,18]. Four candidates have already come to light: $CeRu_4Sn_6$ [19], $Ce_3Bi_4Pd_3$ [20], $CeRu_4Sb_{12}$ [21,22], and YbPtBi [23]. Optical measurements on $CeRu_4Sn_6$ [19] and transport measurements on $CeRu_4Sb_{12}$ [21,22] indicate anisotropic semimetallic behavior. More remarkably, the recent observation of a giant T^3 component to the specific heat of $Ce_3Bi_4Pd_3$ [20] and YbPtBi [23] reveals the presence of point-node excitations.

Recent density-functional calculations [17,24] confirm that heavy fermion systems are expected to host Weyl points with surface Fermi arcs. Lai *et al.* [18] have recently proposed a tight-binding model for hWSMs [18], predicting that the density of states near the Weyl nodes is strongly renormalized by the hybridization with f-electrons. These works raise a number of open questions:

(1) What is the relationship between hWSMs and TKIs?

(2) Beyond renormalization, what are the qualitative effects of strong interactions?

In this paper, we propose a simple a two-band model which links the emergence of hWSMs at the topological quantum critical point (tQCP) between Kondo and TKIs to the development of a parity-breaking on-site hybridization between d and f states in noncentrosymmetric Kondo lattices [Fig. 1(a)].

One of the qualitative effects predicted by our model is the phenomenon of Kondo breakdown, whereby the loss of coordination of local moments at the surface leads to a reduction of the surface Kondo temperature. This phenomenon has been proposed as the origin of light surface quasiparticles observed in SmB_6 [25]. The analogous effect on the Fermi arcs causes them to reconfigure their geometry [Fig. 2] as a function of temperature, giving rise to a strong temperature dependence in the intersurface cyclotron orbits [26–28].

Dzero *et al.* have emphasized that the spin-orbit driven topological behavior in heavy fermion systems derives from the odd-parity hybridization between d (ϕ_d) and f-orbitals (ϕ_f) [1–3] given by the Slater-Koster overlap integral:

$$\tilde{V}_{\alpha\beta}(\mathbf{R}) = \int d^3x \phi^*_{d\alpha}(\mathbf{x}-\mathbf{R})\mathrm{V}(\mathbf{x})\phi_{f\beta}(\mathbf{x}), \qquad (1)$$

where $\mathrm{V}(\mathbf{x})$ is the electronic potential. Inversion symmetry in centrosymmetric crystals fully eliminates the onsite hybridization between the opposite parity d and f states ($V_{\alpha\beta}(0)=0$) [Fig. 1(b)], and in momentum space, the residual intersite components of the hybridization then acquire the odd-in time, odd-in momentum, relativistic form $V_{\alpha\beta}(\mathbf{k}) \sim \mathbf{k}\cdot\vec{\sigma}$ near the high symmetry points. The band crossing permitted by this nodal hybridization drives the formation of TKIs. On the other hand, in noncentrosymmetric crystals, the asymmetric potential $\mathrm{V}(\mathbf{x}) \neq \mathrm{V}(-\mathbf{x})$ distorts the f and d orbitals and eliminates parity conservation, giving rise to a finite onsite d-f hybridization $W_{\alpha\beta} = \tilde{V}_{\alpha\beta}(\mathbf{R}=0)$ [Fig. 1(b)]. Under the influence of this perturbation, TKIs become hWSMs as shown in Fig. 1(a). A minimal model for the hybridization that captures these features in a two-band model is obtained

*pychang@physics.rutgers.edu

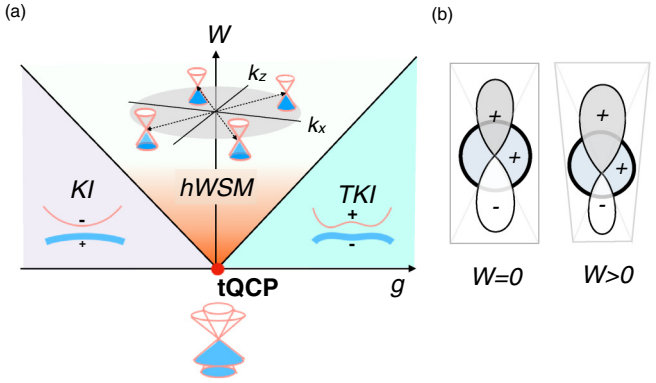

FIG. 1. (a) Topological quantum critical point (tQCP) at the nexus between normal and topological Kondo insulators (KI/TKIs) and heavy Weyl semimetals (hWSMs). g and W are the band tuning and inversion symmetry breaking parameters, respectively. At the tQCP, charge neutrality pins the bulk Dirac cone to the Fermi energy (occupied bands indicated by light blue). Finite $W > 0$ splits the Dirac point into four symmetry-related Weyl points, pinned to the Fermi energy. (b) Breaking of inversion symmetry leads to a finite onsite hybridization $W > 0$.

by generalizing the nearest-neighbor model introduced by Alexandrov, Coleman, and Erten [25] (ACE) to include an additional onsite term as follows:

$$\tilde{V}(\mathbf{R})_{\alpha\beta} = \begin{cases} -i\vec{v}_{\mathbf{R}} \cdot \boldsymbol{\sigma}_{\alpha\beta}, & \mathbf{R} \in \text{n.n.} \\ w_0 + i\vec{w} \cdot \boldsymbol{\sigma} & \mathbf{R} = 0. \end{cases}, \tag{2}$$

where the vector $\vec{v}_{\mathbf{R}} = (v_1 R_1, v_2 R_2, v_3 R_3)$ describes the strength of the nearest neighbor hybridization while w_0 and $\vec{w}$ describe the inversion-symmetry breaking onsite hybridization terms, in a time-reversal invariant form.

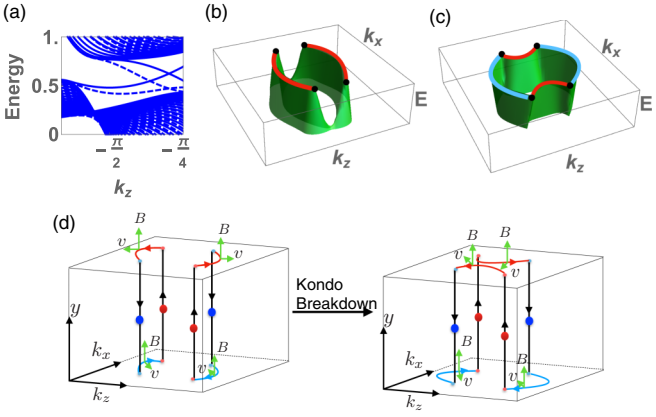

FIG. 2. (a) Kondo Breakdown in a heavy Weyl semimetal, contrasting the spectrum before (solid lines) and after (dashed lines) surface Kondo breakdown as a function of k_z at $k_x = 0$. Surface spectrum (b) before and (c) after surface Kondo breakdown: red and blue lines indicate the Fermi arcs on the top and bottom surfaces, respectively. Black dots indicate the projection of the Weyl nodes onto the surface. Parameters were taken to be $(t_x, t_y, t_z, \mu, \alpha, V_x, V_y, V_z, W_2, b, \lambda) = (2,1,1,-6,-0.1,0.7,0.7,1.05, 0.8,0.89,0.087)$ in Eq. (5). (d) Sche-matic of the Weyl orbits, where arrows indicate the quasiparticle trajectory.

II. MODEL

We use a noncentrosymmetric modification of the ACE model [25]:

$$H = \sum_{i,j,\sigma,\sigma'} \Psi^{\dagger}_{i\sigma} \mathcal{H}_{ij,\sigma\sigma'} \Psi_{j\sigma'} + U \sum_i n_{if\uparrow} n_{if\downarrow}, \tag{3}$$

where

$$\mathcal{H}_{ij,\sigma\sigma'} = \begin{pmatrix} (-t^c_{i,j} - \mu^c \delta_{ij})\delta_{\sigma\sigma'} & \tilde{V}_{\sigma\sigma'}(\mathbf{R}_i - \mathbf{R}_j) \\ \tilde{V}_{\sigma\sigma'}(\mathbf{R}_i - \mathbf{R}_j) & (-t^f_{i,j} - \mu^f \delta_{ij})\delta_{\sigma\sigma'} \end{pmatrix}. \tag{4}$$

Here $\Psi^{\dagger}_{i\sigma} = (c^{\dagger}_{i\sigma}, f^{\dagger}_{i\sigma})$ with $c^{\dagger}_{i\sigma}$ and $f^{\dagger}_{i\sigma}$ are the creation operators for conduction and f-electrons. $t^{c/f}_{ij}$ is the hopping amplitude and $\mu^{c/f}$ is the chemical potential for c/f electrons. U is the onsite Coulomb repulsion between f-electrons.

In the large U limit, a slave-boson approach leads to the mean-field Hamiltonian [29], $H = \sum_{\mathbf{k}} \Psi^{\dagger}(\mathbf{k})\mathcal{H}(\mathbf{k})\Psi(\mathbf{k}) + \mathcal{N}_s \lambda(|b|^2 - Q)$ with

$$\mathcal{H}(\mathbf{k}) = \begin{pmatrix} \epsilon_c(\mathbf{k}) - \mu & \sum_j V_j \sigma_j \sin k_j \\ \sum_j V_j \sigma_j \sin k_j & \epsilon_f(\mathbf{k}) + \lambda \end{pmatrix} + \begin{pmatrix} 0 & W_0 + i\vec{W} \cdot \vec{\sigma} \\ W_0 - i\vec{W} \cdot \vec{\sigma} & 0 \end{pmatrix}. \tag{5}$$

$V_i = v_i b$ and $W_i = w_i b$ are the renormalized hybridization terms, b is the slave boson projection amplitude. The f-hopping amplitude becomes $\tilde{t}^f = b^2 t^f$ The dispersion of the conduction electrons is taken as $\epsilon_c(\mathbf{k}) = -2\sum_i t_i \cos k_i$ and $\epsilon_f(\mathbf{k}) = \alpha\epsilon_c(\mathbf{k})$ for simplicity. The constraint field λ imposes the mean-field constraint $Q = n_f + b^2$ with Q being the local conserved charge associated with the slave boson approach in the infinite U limit, and is taken to be $Q = 1$. $\mathcal{N}_s$ is the total number of sites. We solve the slave-boson mean-field Hamiltonian self-consistently [see Appendix A].

The spectrum of the Hamiltonian [Eq. (5)] is

$$E(\mathbf{k}) = h_0 \pm \sqrt{h_1^2 + W_\mu^2 + \vec{V}_{\mathbf{k}}^2 \pm 2\sqrt{W_\mu^2 \vec{V}_{\mathbf{k}}^2 - (\vec{W} \cdot \vec{V}_{\mathbf{k}})^2}}, \tag{6}$$

where $h_{0/1} = \frac{1}{2}[\epsilon_f(\mathbf{k}) + \lambda \pm (\epsilon_c(\mathbf{k}) - \mu)]$, $W_\mu^2 = W_0^2 + \vec{W}^2$ and $\vec{V}_{\mathbf{k}} = (V_1 \sin k_1, V_2 \sin k_2, V_3 \sin k_3)$.

The energy spectrum has line or point nodes determined by the intersections between three surfaces: $\mathcal{S}_I$ where $h_1 = 0$, $\mathcal{S}_{II}$, where $(W_\mu^2 - \vec{V}_{\mathbf{k}}^2)^2 = 0$, and $\mathcal{S}_{III}$ where $\vec{W} \cdot \vec{V}_{\mathbf{k}} = 0$. When there is no common intersection between these surfaces, the ground state remains a fully gapped insulator. However, once W exceeds a critical value, a semimetallic state develops. There are two cases:

(1) Line-node semimetal ($\vec{W} = 0$), for which the constraint $\mathcal{S}_{III}$ is trivial. Since $\mathcal{S}_I$ and $\mathcal{S}_{II}$ are spheroids that share the same center, they intersect to form two rings $\{r_1, r_2\} = \mathcal{S}_I \cap \mathcal{S}_{II}$ of gapless excitations [Fig. 3(a)] (see Appendix E for the detailed discussion).

(2) Weyl semimetal ($\vec{W} \neq 0$). Here $\mathcal{S}_{III}$ is the plane normal to $\vec{W}$, intersecting with rings $\{r_1, r_2\}$ at four Weyl points [Fig. 3(b)].

Time reversal and reflection symmetries play an important role in Weyl semimetals. Our model preserves time-reversal symmetry, $\mathcal{T}^{-1}\mathcal{H}(\mathbf{k})\mathcal{T} = \mathcal{H}(-\mathbf{k})$, where $\mathcal{T} = i\sigma_2\mathcal{K}$ and $\mathcal{K}$ is

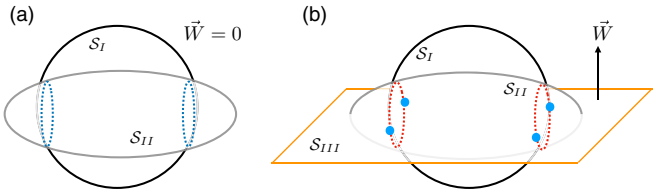

FIG. 3. (a) A line-node semimetal: when $\vec{W}=0$, the line-node solution from Eq. (6) is determined by the intersections $\{r_1,r_2\}=\mathcal{S}_I\cap\mathcal{S}_{II}$ indicated by blue lines. (b) A Weyl semimetal: When $\vec{W}\neq 0$, point-node solutions of Eq. (6), indicated by blue dots, develop at the intersections of plane $\mathcal{S}_{III}$ normal to $\vec{W}$ with the line nodes, $\mathcal{S}_I\cap\mathcal{S}_{II}\cap\mathcal{S}_{III}$.

the conjugation operator. In the absence of W_0, providing the inversion-symmetry breaking vector $\vec{W}=W\hat{l}$ points along a crystal axis $\hat{l}$, then the model also retains reflection symmetries in the two planes with normals $\hat{j}\neq\hat{l}$ perpendicular to $\hat{l}$. For our model, the reflection operator is $\mathcal{R}_j=\sigma_j\tau_3$ and $\mathcal{R}_j^{-1}\mathcal{H}(\mathbf{k})\mathcal{R}_j=\mathcal{H}(\mathbf{k_R})$, where $\mathbf{k_R}$ is the wave vector reflected in the plane perpendicular to $\hat{j}$ and $\boldsymbol{\tau}$ are the Pauli matrices in c,f space. Suppose, for example, $\vec{W}=W_2\hat{y}$, then the energy spectrum has four Weyl points located in the $k_y=0$ plane, each related to one another by time reversal and reflection symmetries $\mathcal{R}_x$ and $\mathcal{R}_z$.

The effective Hamiltonian near the Weyl points is obtained from Eq. (5) by projecting it onto the eigenvectors of the two central bands (see Appendix B). For $\vec{W}=W_2\hat{y}$, we have four Weyl points $\vec{k}_0$, $R_x\vec{k}_0=(-k_{x0},0,k_{z0})$, $R_z\vec{k}_0=(k_{x0},0,-k_{z0})$, and $T\vec{k}_0=-\vec{k}_0$, related by reflection and time-reversal symmetries, respectively. The effective Hamiltonian can be expressed in a general form

$$\mathcal{H}_{\rm eff}(\vec{k}_0,\delta\mathbf{k})=[A(\vec{k}_0)]_{i\alpha}\delta k_i\sigma_\alpha, \tag{7}$$

with implied summation on $i\in[x,y,z]$ and $\alpha\in[0,1,2,3]$ with $\sigma_0=\mathbb{I}_{2\times2}$. Here $[A(\vec{k}_0)]_{i\alpha}$ is a 3×4 matrix defined at each Weyl point $\vec{k}_0$, each proportional to the hybridization amplitudes V_i (see Appendix B). These four effective Hamiltonians are related by reflection and time-reversal symmetries ($R_{x(z)}:\mathcal{H}_{\rm eff}(\vec{k}_0,\delta\mathbf{k})\to\mathcal{H}_{\rm eff}(R_{x(z)}\vec{k}_0,R_{x(z)}\delta\mathbf{k})$ and $T:\mathcal{H}_{\rm eff}(\vec{k}_0,\delta\mathbf{k})\to\mathcal{H}_{\rm eff}(-\vec{k}_0,-\delta\mathbf{k})$), which constrains the four Weyl points to lie at the same energy.

III. KONDO BREAKDOWN

We now examine the effect of "Kondo breakdown" on the Fermi arcs. The topological charges $C=\pm1$ (see Appendix C) associated with the Weyl points give rise to the formation of Fermi arcs, which link the projections of oppositely charged Weyl points onto the surface Brillouin zone (BZ). The analytic form of the localized Fermi arcs can be derived from the effective Hamiltonian (see Appendix D). In the presence of interactions, the reduction in coordination number of the f-elections at the surface suppresses the surface Kondo temperature T_K^* below that of the bulk, $T_K^s<T_K$. In the intermediate temperature regime $T_K^s<T<T_K$, the bulk is topological but the conduction electrons at the surface are liberated from the local moments, leading to surface Kondo breakdown. The surface Kondo breakdown scenario has been confirmed in inhomogeneous mean-field approach [25] and dynamical mean field calculations [30]. To model this effect, we suppress the slave boson amplitude b to zero on the surface layer of hWSMs and recompute the Fermi arcs.

The effect of Kondo breakdown on the surface spectra for a (010) slab geometry is shown in Figs. 2(a)–2(c): we see that the intersections between two surface chiral modes sink beneath the Fermi sea. This effect causes the right and left chiral modes to bulge outwards, leading to a differential reconfiguration of the Fermi arcs on opposite surfaces as shown in Fig. 2(c). In fact, the detailed configuration of the Fermi arcs will in general depend on the microscopic parameters of the Hamiltonian. For example, in $CeRu_4Sn_6$ [17], the nonequivalent cleavage surfaces are found to give rise to different configurations of Fermi arcs. This indicates that the Fermi arcs are sensitive to the surface morphologies and chemical potential. The configuration of the Fermi arcs will also be sensitive to the surface hybridization. Thus the surface Kondo breakdown introduces the reconfiguration of the Fermi arcs. The configuration of the Fermi arcs is a global property of the system, dependent on both bulk and surface properties. In particular, the configuration depends on the locations of the projected Weyl points on the surface BZ and the detailed dispersions of the surface spectrum. On the other hand, the topology of each Weyl point is a local property, with a generic form as described by Eq. (7). The finite topological charge $C=\pm1$ of the Weyl point, ensures the formation of Fermi arcs which link with the projections of oppositely charged Weyl points on the surface BZ. However, this local property does not constrain the way the pairs of oppositely charged Weyl points are linked.

The reconfiguration of the Fermi arcs will have various distinct signatures in both angle-resolved photoemission spectroscopy and quantum oscillation measurements. In a field, quasiparticles on the surface move under the influence of the Lorentz force $\dot{\mathbf{k}}=-e\mathbf{v}_{\rm S}\times\mathbf{B}$, where $\mathbf{v}_{\rm S}$ is their velocity, processing from one projected Weyl point to another. When they reach a Weyl point, the gapless bulk chiral Landau level provides a transport channel to coherently move the quasiparticles between surfaces, giving rise to closed inter-plane Weyl orbits [26,27], as shown in Fig. 2(d). Quantization of the Weyl orbital motion leads to discrete energy levels $E_n=\frac{\pi\hbar(n+\gamma)v_{\rm B}}{L+\beta k_0/(eB)}$, where k_0 is the length of the Fermi arcs, L is the thickness of the sample, γ is a constant, and $\beta=v_{\rm B}/v_{\rm S}$ with $v_{\rm B}$ being the bulk velocity. Such Landau levels have been observed in Shubnikov-de Haas oscillations in Cd_3As_2, a weakly interacting Dirac semimetal which is the crystal-symmetry-protection analogy of a Weyl semimetal [28].

One of the most dramatic consequences of the differential reconfiguration is the merger of two small orbits into a single large orbit as shown in Fig. 2(d), and the effect that will modify the quantum oscillations. Suppose the chemical potential is fixed to be μ and vary the magnetic field B, the nth energy level crosses the μ with the condition

$$\frac{1}{B_n}=\begin{cases}\frac{e}{\beta k_0}\left(\frac{v_{\rm B}\pi\hbar}{\mu}(n+\gamma)-L\right), & T<T_K^s<T_K\\ \frac{e}{\beta'(k_0'+k_1)}\left(\frac{v_{\rm B}\pi\hbar}{\mu}(n+\gamma)-2L\right), & T_K^s<T<T_K\end{cases}, \tag{8}$$

where k_0' and k_1 are the arc-lengths on the bottom and top surfaces respectively [see right panel in Fig. 2(d)], while $\beta'=v_{\rm B}/v_{\rm S}'$ with $v_{\rm S}'$ being the surface velocity of quasiparticles with surface Kondo breakdown.

IV. RENORMALIZATION EFFECTS

During the transition of surface Kondo breakdown, the spacing of the density of states as a function of $1/B$ has a dramatic change, $\omega_{B^{-1}} = \frac{e\pi\hbar v_B}{\beta\mu k_0} \to \frac{e\pi\hbar v_B}{\beta'\mu(k_0'+k_1)}$. The magnetic field $1/B$ threshold of observing this oscillation also changes from $eL/\beta k_0 \to 2eL/\beta'(k_0' + k_1)$. The differential reconfiguration of the Fermi arc states can be detected by measuring the change of oscillation frequency and a threshold of the magnetic field in Shubnikov-de Haas oscillations.

The renormalized velocity of the Weyl semimetals described in Eq. (7) is proportional to the hybridization amplitude $V_i \propto \sqrt{T_K D}$ where T_K is the Kondo temperature and D is the band width of the conduction electrons [31]. This "square-root" renormalization effect is weaker than that seen in heavy fermion metals, due to the hybridization origin of the nodes. From Ref. [17], the velocity of Weyl fermion in $CeRu_4Sn_6$ is $v^* \sim 0.2$ eVÅ. For the weakly interacting Weyl semimetals such as TaAs [32] and TaP [14], the velocity of Weyl fermion $v \sim 2 - 3$ eVÅ. The renormalization effect in hWSMs is about a factor of 10.

Many of the thermodynamic and transport properties in hWSMs are affected by this quasiparticle renormalization effect. One of the most dramatic effects, is the renormalization of the cubic specific heat. A large T^3 specific heat has been reported in the candidate hWSM materials $Ce_3Bi_4Pd_3$ [20] and YbPtBi [23]. As pointed out by Lai *et al.* [18] this significant enhancement of specific heat likely derives from the cubic dependence on renormalized velocity $C_v = \frac{\partial}{\partial T}\int \epsilon f(\epsilon) g(\epsilon) d\epsilon \propto (T/v^*)^3$ with $g(\epsilon) = \frac{\epsilon^2}{2\pi^2 v^{*3}}$ being the density of states. In addition to the specific heat, an enhancement of the high-field thermopower [33] is also expected. The high-field thermoelectric properties of the Weyl/Dirac semimetals contrast dramatically with those of doped semiconductors, with a thermopower that grows linearly, without saturation, in a the magnetic field, $\alpha := \Delta V/\Delta T \propto BT/v^*$, where ΔV and ΔT are the voltage and temperature difference, respectively. The nonsaturating behavior leads to a large thermopower which has been observed in weakly interacting Dirac semimetal $Pb_{1-x}Sn_xSe$ [34]. The high-field thermopower is thus enhanced by the mass renormalization in hWSMs.

V. CONCLUSION AND DISCUSSION

We have proposed a hybridization-driven model for hWSMs, arguing that the onsite hybridization between f and d orbitals in noncentrosymmetric crystals drives TKIs into hWSMs. One of the effects of the strong interactions is surface Kondo breakdown, which leads to a reconfiguration of Fermi arcs on both surfaces that should appear in quantum oscillations, while the renormalization of velocity in hWSMs affects thermodynamic and transport properties.

There are a number of interesting new directions for research into hWSMs that deserve mention. One aspect that deserves exploration is the influence of nonsymmorphic space group symmetries. According to topological band theory [35], such symmetries can lead to nodal points with much higher multiplicities, giving rise to a cluster of nested Dirac cones. A particularly interesting case is the candidate hWSM $Ce_3Bi_4Pd_3$, the space group No. 220 ($I\bar{4}3d$) is expected to produce an eightfold degenerate double Dirac point. These nodal lines are expected to give rise to "drumhead surface states" [13,36,37] (see Appendix E), which can potentially cause charge/spin-density wave and superconducting instabilities. A second interesting direction is the possible use of molecular beam epitaxy techniques [38], which open up the possibility of artificially engineered hWSMs, where tuning the degree of inversion symmetry breaking can be used to explore the vicinity, and possible instabilities of the tQCP [39,40].

ACKNOWLEDGMENTS

The authors would like to thank J. Analytis, E. König, S. Paschen, and Y. Xu for valuable discussions. This paper was supported by the Rutgers Center for Materials Theory group postdoc grant (P.-Y.C.) and US Department of Energy Grant No. DE-FG02-99ER45790 (P.C.).

APPENDIX A: SELF-CONSISTENT SLAVE BOSON MEAN-FIELD SOLUTIONS

In the large U limit, a slave-boson approach leads to the mean-field Hamiltonian [29], $H = \sum_{\mathbf{k}} \Psi^\dagger(\mathbf{k})\mathcal{H}(\mathbf{k})\Psi(\mathbf{k}) + \mathcal{N}_s\lambda(|b|^2 - Q)$ with

$$\mathcal{H}(\mathbf{k}) = \begin{pmatrix} \epsilon_c(\mathbf{k}) - \mu & \sum_j V_j\sigma_j \sin k_j \\ \sum_j V_j\sigma_j \sin k_j & \epsilon_f(\mathbf{k}) + \lambda \end{pmatrix} + \begin{pmatrix} 0 & W_0 + i\vec{W}\cdot\vec{\sigma} \\ W_0 - i\vec{W}\cdot\vec{\sigma} & 0 \end{pmatrix}. \tag{A1}$$

$V_i = v_i b$ and $W_i = w_i b$ are the renormalized hybridization terms, b is the slave boson projection amplitude. The f-hopping amplitude becomes $\tilde{t}^f = b^2 t^f$. The dispersion of the conduction electrons is taken as $\epsilon_c(\mathbf{k}) = -2\sum_i t_i \cos k_i$ and $\epsilon_f(\mathbf{k}) = \alpha\epsilon_c(\mathbf{k})$ for simplicity. The constraint field λ imposes the mean-field constraint $Q = n_f + b^2$ with Q being the local conserved charge associated with the slave boson approach in the infinite U limit, and is taken to be $Q = 1$. $\mathcal{N}_s$ is the total number of sites.

The saddle point equations can be obtained from $\frac{\delta\langle H\rangle}{\delta b} = 0$ and $\frac{\delta\langle H\rangle}{\delta\lambda} = 0$.

$$\frac{1}{\mathcal{N}_s}\sum_{\mathbf{k},\sigma}\langle f^\dagger_{\mathbf{k},\sigma} f_{\mathbf{k},\sigma}\rangle + b^2 = 1, \tag{A2}$$

$$\frac{1}{2\mathcal{N}_s}\sum_{\mathbf{k},\sigma,i,j,\alpha,\beta}\{(v_i \sin k_i[\sigma_i]_{\alpha\beta} + w_0\delta_{\alpha\beta} + i w_j[\sigma_j]_{\alpha\beta}), \tag{A3}$$

$$\langle c^\dagger_{\mathbf{k},\alpha} f_{\mathbf{k},\beta}\rangle + \text{H.c.}\} + b\left(\lambda - \frac{1}{\mathcal{N}_s}\sum_{\mathbf{k},\sigma}\langle\tilde{\epsilon}_f(\mathbf{k}) f^\dagger_{\mathbf{k},\sigma} f_{\mathbf{k},\sigma}\rangle\right) = 0, \tag{A4}$$

where $\tilde{\epsilon}_f(\mathbf{k}) = \frac{1}{b^2}\epsilon_f(\mathbf{k})$ is the bare spectrum of the f-electron.

In the paper, we consider the case of nonzero on-site hybridization $w_2 \neq 0$. For the specific calculations carried out in the paper, we have chosen the bare parameter values to be $(v_x, v_y, v_z, w_2, \alpha, t_x, t_y, t_z, \mu) = (0.786, 0.786, 1.179, 0.89, -0.126, 2, 1, 1, -6)$, leading to a self-consistently determined slave boson amplitude and the constraint field with values $(b, \lambda) = (0.89, 0.087)$.

APPENDIX B: EFFECTIVE TWO-DIMENSIONAL HAMILTONIAN NEAR THE WEYL POINTS

Now we analyze the effective Hamiltonian around the Weyl points. We consider the inversion breaking hybridization $W_2 \neq 0$ such that the Weyl points are located at $k_y = 0$ plane. The locations of the Weyl points in momentum space satisfy

$$\begin{aligned} &-2t_x \cos k_{x0} - 2t_z \cos k_{z0} - (\mu + 2t_y) = 0, \\ &W_2^2 = V_1^2 \sin^2 k_{x0} + V_3^2 \sin^2 k_{z0}. \end{aligned} \tag{B1}$$

We can expand the Hamiltonian around the Weyl points up to linear terms in $\mathbf{k}$.

$$\mathcal{H}(\delta\mathbf{k}) \sim \mathcal{H}_0 + \mathcal{H}_1(\delta\mathbf{k}), \tag{B2}$$

where

$$\mathcal{H}_0 = [V_1(\sin k_{x0})\sigma_1 + V_3(\sin k_{z0})\sigma_3]\tau_1 + W_2\sigma_2\tau_2, \tag{B3}$$

and

$$\begin{aligned} \mathcal{H}_1(\delta\mathbf{k}) =& \tfrac{1}{2}(1+\alpha)[2t_x \sin k_{x0}\delta k_x + 2t_z \sin k_{z0}\delta k_z]\tau_3 \\ &+ [V_1(\cos k_{x0}\delta k_x)\sigma_1 + V_2\delta k_y \\ &+ V_3(\cos k_{z0}\delta k_z)\sigma_3]\tau_1. \end{aligned} \tag{B4}$$

Here we have dropped terms proportional to the identity matrix, which only shift the spectrum without changing the band topology. To obtain the effective two-dimensional Hamiltonian in the vicinity of the Weyl points we first find two eigenvectors of $\mathcal{H}_0$ with zero energy,

$$\begin{aligned} |v_1\rangle =& \frac{1}{\sqrt{2\left(V_{1,k_{x0}}^2 + V_{3,k_{z0}}^2\right) + 2V_{1,k_{x0}}\sqrt{V_{1,k_{x0}}^2 + V_{3,k_{z0}}^2}}} \\ &\begin{pmatrix} V_{1,k_{x0}} + \sqrt{V_{1,k_{x0}}^2 + V_{3,k_{z0}}^2} \\ 0 \\ -V_{3,k_{z0}} \\ 0 \end{pmatrix}, \\ |v_2\rangle =& \frac{1}{\sqrt{2\left(V_{1,k_{x0}}^2 + V_{3,k_{z0}}^2\right) + 2V_{1,k_{x0}}\sqrt{V_{1,k_{x0}}^2 + V_{3,k_{z0}}^2}}} \\ &\begin{pmatrix} 0 \\ V_{3,k_{z0}} \\ 0 \\ V_{1,k_{x0}} + \sqrt{V_{1,k_{x0}}^2 + V_{3,k_{z0}}^2} \end{pmatrix}, \end{aligned} \tag{B5}$$

where $V_{1(3),k_{x/z0}} = V_{1(3)} \sin k_{x(z)0}$,and $V_{2,k_{y0}} = V_2$ with $\vec{k}_0$ being the position of the Weyl point.

The effective two-dimensional Hamiltonian is then obtained by projecting the Hamiltonian onto these eigenvalues, $[\mathcal{H}_{\text{eff}}]_{i,j} = \langle v_i|\mathcal{H}_1(\delta\mathbf{k})|v_j\rangle$ with $i,j = 1,2$, giving rise to

$$\begin{aligned} \mathcal{H}_{\text{eff}}(\delta\mathbf{k}) =& -h_{0,\vec{k}_0}\sigma_z - V_{2,k_{y0}}\delta k_y\sigma_x \\ &+ \frac{V_{1,k_{x0}} + \sqrt{V_{1,k_{x0}}^2 + V_{3,k_{z0}}^2}}{V_{1,k_{x0}}^2 + V_{3,k_{z0}}^2 + V_{1,k_{x0}}\sqrt{V_{1,k_{x0}}^2 + V_{3,k_{z0}}^2}} \\ &\times [V_{1,k_{x0}}\tilde{V}_{1,k_{x0}}\delta k_x + V_{3,k_{z0}}\tilde{V}_{3,k_{z0}}\delta k_z]\sigma_y, \end{aligned} \tag{B6}$$

where $h_{0,\vec{k}_0} = \frac{1}{2}(1+\alpha)[2t_x \sin k_{x0}\delta k_x + 2t_z \sin k_{z0}\delta k_z]$, and $\tilde{V}_{1(3),k_{x(z)0}} = V_{1(3)} \cos k_{x(z)0}$.

For simplicity, we express the Hamiltonian as

$$\begin{aligned} \mathcal{H}_{\text{eff}}(\delta\mathbf{k}) =& (A\delta k_x + B\delta k_z)\sigma_z \\ &+ (C\delta k_x + D\delta k_z)\sigma_y + E\delta k_y\sigma_x, \end{aligned} \tag{B7}$$

where

$$\begin{aligned} A =& -\frac{1+\alpha}{2}(2t_x \sin k_{x0}), \quad B = -\frac{1+\alpha}{2}(2t_z \sin k_{z0}) \\ C =& \frac{V_{1,k_{x0}} + \sqrt{V_{1,k_{x0}}^2 + V_{3,k_{z0}}^2}}{V_{1,k_{x0}}^2 + V_{3,k_{z0}}^2 + V_{1,k_{x0}}\sqrt{V_{1,k_{x0}}^2 + V_{3,k_{z0}}^2}} V_{1,k_{x0}}\tilde{V}_{1,k_{x0}}, \\ D =& \frac{V_{1,k_{x0}} + \sqrt{V_{1,k_{x0}}^2 + V_{3,k_{z0}}^2}}{V_{1,k_{x0}}^2 + V_{3,k_{z0}}^2 + V_{1,k_{x0}}\sqrt{V_{1,k_{x0}}^2 + V_{3,k_{z0}}^2}} V_{3,k_{z0}}\tilde{V}_{3,k_{z0}}, \\ E =& -V_{2,k_{y0}}. \end{aligned} \tag{B8}$$

APPENDIX C: TOPOLOGICAL INVARIANCE OF THE WEYL POINTS—BERRY CURVATURE

The topological invariance of the Weyl points is the Berry curvature computed from a two-dimensional surface encircling the Weyl point. The definition of the Berry curvature is

$$C = \frac{i}{2\pi}\sum_{\alpha\in\text{occ}}\int d^2k\langle\partial_{k_i}u_\alpha|\partial_{k_j}u_\alpha\rangle - (k_i \leftrightarrow k_j), \tag{C1}$$

where u_α are the occupied bands and the two-dimensional integral is a closed surface around one Weyl point.

Now we compute the Berry curvature around the Weyl point by using Eq. (B6). Without loss of generality, we define $\tilde{k}_x = A\delta k_x + B\delta k_z$, $\tilde{k}_z = C\delta k_x + D\delta k_z$, and $\tilde{k}_y = E\delta k_y$.

We now choose a fixed radius R around the Weyl point with $R^2 = \sum_{i=x,y,z}\tilde{k}_i^2$. The occupied band with energy $-R$ is

$$u_-(\theta,\phi) = \begin{pmatrix} -\sin\frac{\theta}{2}e^{-i\phi} \\ \cos\frac{\theta}{2} \end{pmatrix}, \tag{C2}$$

where we parametrize $\tilde{k}_z = R\cos\theta$, $\tilde{k}_x = R\sin\theta\cos\phi$, and $\tilde{k}_y = R\sin\theta\sin\phi$.

The only nonvanishing component of the Berry connection is

$$A_\phi = \frac{1}{R\sin\theta}\langle u_-(\theta,\phi)|\partial_\phi u_-(\theta,\phi)\rangle = \frac{i}{2R}\cot\theta. \tag{C3}$$

The Berry curvature around the Weyl point is then

$$C = \frac{i}{2\pi}\int_{\text{sphere}} ds(\nabla\times\vec{A}) = \frac{i}{2\pi}\int R^2\sin\theta d\theta d\phi\frac{-i}{2R^2} = 1. \tag{C4}$$

The Berry curvature of the the other time-reversal related Weyl points at $-\vec{k}_0$, is $C = -1$.

APPENDIX D: FERMI ARC STATES IN THE EFFECTIVE HAMILTONIAN

We analyze the Fermi arc state from the effective two-dimensional Hamiltonian in Eq. (B6). In the presence of (010) surface, the effective Hamiltonian around the Weyl point is expressed as

$$\mathcal{H}_{\text{eff}} = \begin{pmatrix} A\delta k_x + B\delta k_z & -iC\delta k_x - iD\delta k_z - iE\partial_y \\ iC\delta k_x + iD\delta k_z - iE\partial_y & -A\delta k_x - B\delta k_z \end{pmatrix}. \tag{D1}$$

We consider a cylindrical surface surrounding the Weyl point with radius k_0. The effective Hamiltonian becomes

$$\mathcal{H}_{\text{eff}} = \begin{pmatrix} Ak_0\cos\theta + Bk_0\sin\theta & -ik_0\sqrt{C^2+D^2}\cos(\theta-\phi) - iE\partial_y \\ ik_0\sqrt{C^2+D^2}\cos(\theta-\phi) - iE\partial_y & -Ak_0\cos\theta - Bk_0\sin\theta \end{pmatrix}, \tag{D2}$$

where $\phi = \cos^{-1}\frac{C}{\sqrt{C^2+D^2}}$, $\delta k_x = k_0\cos\theta$, and $\delta k_z = k_0\sin\theta$.

There are two boundary states on this cylinder surrounding the Weyl point

$$\begin{aligned} u_{y>0} &= \begin{pmatrix} 1 \\ 0 \end{pmatrix}\sqrt{2\kappa}e^{-\kappa y} \quad \text{with} \quad E_R(\theta) = Ak_0\cos\theta + Bk_0\sin\theta, \\ u_{y<0} &= \begin{pmatrix} 0 \\ 1 \end{pmatrix}\sqrt{2\kappa}e^{\kappa y} \quad \text{with} \quad E_L(\theta) = -Ak_0\cos\theta - Bk_0\sin\theta, \end{aligned} \tag{D3}$$

where $\kappa = -\frac{k_0}{E}\sqrt{C^2+D^2}\cos(\theta-\phi) > 0$. These boundary states are the origin of the Fermi arc states.

APPENDIX E: TIME-REVERSAL SYMMETRIC NODAL RING SEMIMETALLIC PHASE

The Hamiltonian of hWSMs with nonvanishing W_0 can be expressed as

$$\mathcal{H}(\mathbf{k}) = \mathcal{H}_0(\mathbf{k}) + \mathcal{H}_1(\mathbf{k}), \tag{E1}$$

where $\mathcal{H}_0(\mathbf{k}) = \frac{1}{2}(\epsilon_c(\mathbf{k}) + \epsilon_f(\mathbf{k}))\sigma_0\tau_0$ and $\mathcal{H}_1(\mathbf{k}) = \frac{1}{2}(\epsilon_c(\mathbf{k}) - \epsilon_f(\mathbf{k}))\sigma_0\tau_3 + \sum_{i=1,2,3} V_i \sin k_i\sigma_i\tau_1 + W_0\tau_1$. $\mathcal{H}_1(\mathbf{k})$ has a chiral symmetry, $\mathcal{S}^{-1}\mathcal{H}(\mathbf{k})\mathcal{S} = -\mathcal{H}(\mathbf{k})$, where $\mathcal{S} = \tau_2$. In the presence of chiral symmetry, one can off-block diagonalize $\mathcal{H}_1(\mathbf{k})$ by a unitary transformation, $\mathcal{V}^\dagger\mathcal{H}_1(\mathbf{k})\mathcal{V} = \tilde{\mathcal{H}}_1(\mathbf{k})$, where

$$\mathcal{V} = \frac{1}{\sqrt{2}}\begin{pmatrix} \mathbb{I}_{2\times2} & i\mathbb{I}_{2\times2} \\ i\mathbb{I}_{2\times2} & \mathbb{I}_{2\times2} \end{pmatrix}, \quad \tilde{\mathcal{H}}(\mathbf{k})_1 = \begin{pmatrix} 0 & D(\mathbf{k}) \\ D^\dagger(\mathbf{k}) & 0 \end{pmatrix}, \tag{E2}$$

with $D(\mathbf{k}) = i(\epsilon_c(\mathbf{k}) - \epsilon_f(\mathbf{k})) + 2\sum_i V_i \sin k_i\sigma_i + m_0$. The eigenvectors of $\tilde{\mathcal{H}}(\mathbf{k})$ satisfy

$$\begin{pmatrix} 0 & D(\mathbf{k}) \\ D^\dagger(\mathbf{k}) & 0 \end{pmatrix}\begin{pmatrix} \chi^\pm(\mathbf{k}) \\ \eta^\pm(\mathbf{k}) \end{pmatrix} = \pm\lambda(\mathbf{k})\begin{pmatrix} \chi^\pm(\mathbf{k}) \\ \eta^\pm(\mathbf{k}) \end{pmatrix}. \tag{E3}$$

These eigenvectors are also the eigenvector of $\mathcal{H}_0(\mathbf{k})$ and they determine the topological invariant. We pick $\chi^\pm(\mathbf{k}) = \frac{1}{\sqrt{2}}u(\mathbf{k})$, Then Eq. (E3) leads to $\eta^\pm(\mathbf{k}) = \pm\frac{1}{\sqrt{2}}\frac{1}{\lambda(\mathbf{k})}D^\dagger(\mathbf{k})u(\mathbf{k})$. The flat band Hamiltonian $\mathcal{Q}(\mathbf{k})$can be obtained from the projector

$$\begin{aligned} \mathcal{Q}(\mathbf{k}) =& \mathbb{I} - 2\sum_{\alpha\in\text{occ}} |u_\alpha(\mathbf{k})\rangle\langle u_\alpha(\mathbf{k})| \\ =& \mathbb{I} - \begin{pmatrix} u(\mathbf{k}) \\ -\frac{1}{\lambda(\mathbf{k})}D^\dagger(\mathbf{k})u(\mathbf{k}) \end{pmatrix}\begin{pmatrix} u^\dagger(\mathbf{k}) & -\frac{1}{\lambda(\mathbf{k})}u^\dagger(\mathbf{k})D(\mathbf{k}) \end{pmatrix} \\ =& \frac{1}{\lambda(\mathbf{k})}\begin{pmatrix} 0 & u(\mathbf{k})u^\dagger(\mathbf{k})D(\mathbf{k}) \\ D^\dagger(\mathbf{k})u(\mathbf{k})u^\dagger(\mathbf{k}) & 0 \end{pmatrix} \\ =& \begin{pmatrix} 0 & q(\mathbf{k}) \\ q^\dagger(\mathbf{k}) & 0 \end{pmatrix}. \end{aligned} \tag{E4}$$

The topological invariance of the nodal ring is characterized by a winding number of a one-dimensional loop encircling the ring. The winding number can be calculated from the q-matrix integral

$$\nu = \frac{1}{2\pi i}\oint_{\mathcal{L}} d\mathbf{k}\,\text{Tr}[q^{-1}(\mathbf{k})\partial_{\mathbf{k}}q(\mathbf{k})]. \tag{E5}$$

In our model, the winding number of the nodal rings is $\nu = \pm1$, which leads to surface flat bands bounded by the nodal rings projected on the surface Brillouin zone [13,36]. As shown schematically in Fig. 4(a), two nodal rings are centered along k_y axis. On (011) surface, the flat band surface states emerge inside the bulk rings projected on the (011) surface Brillouin zone.

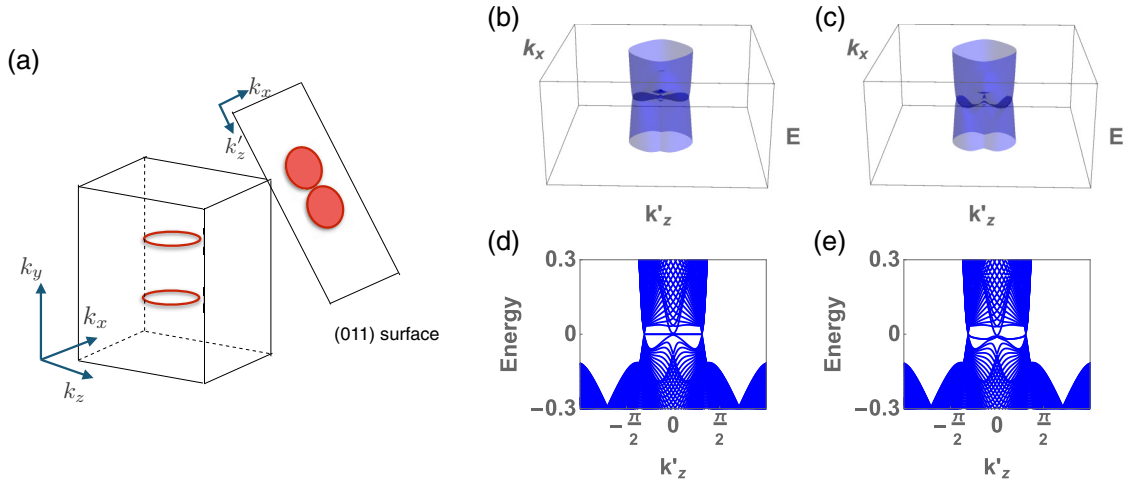

FIG. 4. (a) Schematic plot of the bulk nodal rings centered at k_y axis. On the (011) surface, the surface flat bands will emerge inside the circles which are the projection of the bulk nodal rings. The surface spectrum as a function of $(k_x, k'_z = \frac{1}{\sqrt{2}}(k_z - k_y))$ from the Hamiltonian Eq. (5) with $(t_x, t_y, t_z, \mu, \alpha, W_x, W_y, W_z, W_0) = (2,1,1,-6.5,-0.1,2,2,2,1.8)$. (b) in the absence of surface Kondo breakdown and (c) in the presence of surface Kondo breakdown. The surface spectrum as a function of $k'_z = \frac{1}{\sqrt{2}}(k_z - k_y)$ at $k_x = 0$, (d) in the absence of surface Kondo breakdown, and (e) in the presence of surface Kondo breakdown.

Finally, we have investigated the Kondo breakdown on these surface flat bands, summarizing the results in 4. In the absence of the surface Kondo breakdown, the surface flat bands emerge on (011) surface [Figs. 4(b) and 4(d)]. In the presence of the surface Kondo breakdown, the surface flat bands sink beneath the Fermi sea as shown in Figs. 4(c) and 4(c).

[1] N. Mott, Philos. Mag. **30**, 403 (1974).
[2] M. Dzero, K. Sun, V. Galitski, and P. Coleman, Phys. Rev. Lett. **104**, 106408 (2010).
[3] M. Dzero, K. Sun, P. Coleman, and V. Galitski, Phys. Rev. B **85**, 045130 (2012).
[4] V. Alexandrov, M. Dzero, and P. Coleman, Phys. Rev. Lett. **111**, 226403 (2013).
[5] F. Lu, J. Z. Zhao, H. Weng, Z. Fang, and X. Dai, Phys. Rev. Lett. **110**, 096401 (2013).
[6] M. Dzero, J. Xia, V. Galitski, and P. Coleman, Annu. Rev. Condens. Matter Phys. **7**, 249 (2016).
[7] J. Jiang, S. Li, T. Zhang, Z. Sun, F. Chen, Z. R. Ye, M. Xu, Q. Q. Ge, S. Y. Tan, X. H. Niu, M. Xia, B. P. Xie, Y. F. Li, X. H. Chen, H. H. Wen, and D. L. Feng, Nat. Commun. **4**, 3010 (2013).
[8] M. Neupane, N. Alidoust, S.-Y. Xu, T. Kondo, Y. Ishida, D. J. Kim, C. Liu, I. Belopolski, Y. J. Jo, T.-R. Chang, H.-T. Jeng, T. Durakiewicz, L. Balicas, H. Lin, A. Bansil, S. Shin, Z. Fisk, and M. Z. Hasan, Nat. Commun. **4**, 2991 (2013).
[9] N. Xu, X. Shi, P. K. Biswas, C. E. Matt, R. S. Dhaka, Y. Huang, N. C. Plumb, M. Radović, J. H. Dil, E. Pomjakushina, K. Conder, A. Amato, Z. Salman, D. M. Paul, J. Mesot, H. Ding, and M. Shi, Phys. Rev. B **88**, 121102 (2013).
[10] E. Frantzeskakis, N. de Jong, B. Zwartsenberg, Y. K. Huang, Y. Pan, X. Zhang, J. X. Zhang, F. X. Zhang, L. H. Bao, O. Tegus, A. Varykhalov, A. de Visser, and M. S. Golden, Phys. Rev. X **3**, 041024 (2013).
[11] S. Murakami, New J. Phys. **9**, 356 (2007).
[12] X. Wan, A. M. Turner, A. Vishwanath, and S. Y. Savrasov, Phys. Rev. B **83**, 205101 (2011).
[13] A. A. Burkov and L. Balents, Phys. Rev. Lett. **107**, 127205 (2011).
[14] S.-Y. Xu, I. Belopolski, D. S. Sanchez, C. Zhang, G. Chang, C. Guo, G. Bian, Z. Yuan, H. Lu, T.-R. Chang, P. P. Shibayev, M. L. Prokopovych, N. Alidoust, H. Zheng, C.-C. Lee, S.-M. Huang, R. Sankar, F. Chou, C.-H. Hsu, H.-T. Jeng, A. Bansil, T. Neupert, V. N. Strocov, H. Lin, S. Jia, and M. Z. Hasan, Sci. Adv. **1**, e1501092 (2015).
[15] H. Weng, C. Fang, Z. Fang, B. A. Bernevig, and X. Dai, Phys. Rev. X **5**, 011029 (2015).
[16] S.-M. Huang, S.-Y. Xu, I. Belopolski, C.-C. Lee, G. Chang, B. Wang, N. Alidoust, G. Bian, M. Neupane, C. Zhang, S. Jia, A. Bansil, H. Lin, and M. Z. Hasan, Nat. Commun. **6**, 7373 (2015).
[17] Y. Xu, C. Yue, H. Weng, and X. Dai, Phys. Rev. X **7**, 011027 (2017).
[18] H.-H. Lai, S. E. Grefe, S. Paschen, and Q. Si, Proc. Natl. Acad. Sci. USA **115**, 93 (2018).
[19] V. Guritanu, P. Wissgott, T. Weig, H. Winkler, J. Sichelschmidt, M. Scheffler, A. Prokofiev, S. Kimura, T. Iizuka, A. M. Strydom, M. Dressel, F. Steglich, K. Held, and S. Paschen, Phys. Rev. B **87**, 115129 (2013).
[20] S. Dzsaber, L. Prochaska, A. Sidorenko, G. Eguchi, R. Svagera, M. Waas, A. Prokofiev, Q. Si, and S. Paschen, Phys. Rev. Lett. **118**, 246601 (2017).
[21] H. Okamura, R. Kitamura, M. Matsunami, H. Sugawara, H. Harima, H. Sato, T. Moriwaki, Y. Ikemoto, and T. Nanba, J. Phys. Soc. Jpn. **80**, 084718 (2011).
[22] A. Shankar, D. P. Rai, S. Chettri, R. Khenata, and R. K. Thapa, J. Solid State Chem. France **240**, 126 (2016).

[23] C. Y. Guo, F. Wu, M. Smidman, F. Steglich, and H. Q. Yuan, arXiv:1710.05522 [cond-mat.str-el].
[24] P. Wissgott and K. Held, Eur. Phys. J. B **89**, 5 (2016).
[25] V. Alexandrov, P. Coleman, and O. Erten, Phys. Rev. Lett. **114**, 177202 (2015).
[26] X. Dai, Nat. Phys. **12**, 727 (2016).
[27] A. C. Potter, I. Kimchi, and A. Vishwanath, Nat. Commun. **5**, 5161 (2014).
[28] P. J. W. Moll, N. L. Nair, T. Helm, A. C. Potter, I. Kimchi, A. Vishwanath, and J. G. Analytis, Nature (London) **535**, 266 (2016).
[29] P. Coleman, Phys. Rev. B **35**, 5072 (1987).
[30] R. Peters, T. Yoshida, H. Sakakibara, and N. Kawakami, Phys. Rev. B **93**, 235159 (2016).
[31] P. Coleman, *Introduction to Many-Body Physics* (Cambridge University Press, Cambridge, 2015).
[32] B. Q. Lv, H. M. Weng, B. B. Fu, X. P. Wang, H. Miao, J. Ma, P. Richard, X. C. Huang, L. X. Zhao, G. F. Chen, Z. Fang, X. Dai, T. Qian, and H. Ding, Phys. Rev. X **5**, 031013 (2015).
[33] B. Skinner and L. Fu, arXiv:1706.06117 [cond-mat.str-el].
[34] T. Liang, Q. Gibson, J. Xiong, M. Hirschberger, S. P. Koduvayur, R. J. Cava, and N. P. Ong, Nat. Commun. **4**, 2696 (2013).
[35] B. Bradlyn, J. Cano, Z. Wang, M. G. Vergniory, C. Felser, R. J. Cava, and B. A. Bernevig, Science **353**, aaf5037 (2016).
[36] S. Matsuura, P.-Y. Chang, A. P. Schnyder, and S. Ryu, New J. Phys. **15**, 065001 (2013).
[37] G. Bian, T.-R. Chang, H. Zheng, S. Velury, S.-Y. Xu, T. Neupert, C.-K. Chiu, S.-M. Huang, D. S. Sanchez, I. Belopolski, N. Alidoust, P.-J. Chen, G. Chang, A. Bansil, H.-T. Jeng, H. Lin, and M. Z. Hasan, Phys. Rev. B **93**, 121113 (2016).
[38] T. Ishii, R. Toda, Y. Hanaoka, Y. Tokiwa, M. Shimozawa, Y. Kasahara, R. Endo, T. Terashima, A. H. Nevidomskyy, T. Shibauchi, and Y. Matsuda, Phys. Rev. Lett. **116**, 206401 (2016).
[39] B.-J. Yang, E.-G. Moon, H. Isobe, and N. Nagaosa, Nat. Phys. **10**, 774 (2014).
[40] H. Isobe and L. Fu, Phys. Rev. B **93**, 241113 (2016).